Measurement of the Total Energy Release Rate for Cracks in PZT Under Combined Mechanical and Electrical Loading

H. Jelitto

F. Felten[1]

Institute of Advanced Ceramics,
Hamburg University of Technology,
Denickestrasse 15,
D-21073 Hamburg, Germany

M. V. Swain
Biomaterials,
Faculty of Dentistry,
University of Sydney,
Sydney 2010, Australia

H. Balke
Technische Universität Dresden,
Institut für Festkörpermechanik,
D-01062 Dresden, Germany

G. A. Schneider
Institute of Advanced Ceramics,
Hamburg University of Technology,
Denickestrasse 15,
D-21073 Hamburg, Germany

Four-point-bending V-notched specimens of lead zirconate titanate (PZT) poled parallel to the long axis are fractured under conditions of controlled crack growth in a custom-made device. In addition to the mechanical loading electric fields, up to 500 V/mm *are applied parallel and anti-parallel to the poling direction, i.e., perpendicular to the crack surface. To determine the different contributions to the total energy release rate, the mechanical and the piezoelectric compliance, as well as the electrical capacitance of the sample, are recorded continuously using small signal modulation/demodulation techniques. This allows for the calculation of the mechanical, the piezoelectric, and the electrical part of the total energy release rate due to linear processes. The sum of these linear contributions during controlled crack growth is attributed to the intrinsic toughness of the material. The nonlinear part of the total energy release rate is mostly associated to domain switching leading to a switching zone around the crack tip. The measured force-displacement curve, together with the modulation technique, enables us to determine this mechanical nonlinear contribution to the overall toughness of PZT. The intrinsic material toughness is only slightly dependent on the applied electric field (10% effect), which can be explained by screening charges or electrical breakdown in the crack interior. The part of the toughness due to inelastic processes increases from negative to positive electric fields by up to 100%. For the corresponding nonlinear electric energy change during crack growth, only a rough estimate is performed.*
[DOI: 10.1115/1.2744027]

Keywords: PZT, piezoelectric, fracture criterion, compliance, energy release rate

1 Introduction

Piezoelectric ceramics are commonly used as sensors and actuators in versatile, technical fields, such as the automotive industry, medical technology, metrology, and sonar applications [1]. In this context, the reliability is of particular importance, as such ceramics are susceptible to brittle fracture [2]. Because of their piezoelectric properties, in most applications these ceramics are used under combined mechanical and electrical loads. A large number of theoretical papers have been published concerning the influence of electric fields on cracks in piezoelectric materials [3–7]. Most approaches predict strong effects in retarding crack growth when an electric field is applied perpendicular to a nonconducting crack. On the other hand, experimental work has shown that the theoretically predicted effects are greatly overestimated and even partially contradictory to the experimental results. It seems evident that the fracture toughness in poled ferroelectric ceramics is larger for crack growth parallel to the polarization direction than perpendicular to it, which is related to ferroelastic domain switching. Moreover, concerning the influence of an additional electric field, different effects were reported that have not lead to a consistent understanding until now [8–13]. However, the evaluation of these experiments is difficult because of the nonlinear ferroic behavior, and also appropriate assumptions of the electrical boundary conditions of the crack are necessary to describe fracture in piezoelectric materials. The theoretical description of nonconducting cracks is often based on the assumption of complete impermeability. This is a major simplification, because electrical discharge and crack geometry effects such as bridging and branching elevates the permittivity interior to the crack significantly, as found by Schneider et al. [14]. Hence, finding an adequate fracture criterion that takes both mechanical and electrical loads into account is still one of the most challenging issues.

A critical value of the total energy release rate is used for one of the potential fracture criteria, as it is based on thermodynamic considerations [6,7]. Thus, a crack will start to propagate when a critical value $\mathcal{G}_c$ is reached, which is related to the surface energy of the material and the energy dissipation in the process zone. In several theoretical papers, the total, as well as the crack tip energy release rate, has been calculated for different geometries and under different assumptions regarding the electrical boundary conditions [3,5,7,8,15–17]. However, there is still a lack of experimental data to evaluate the theoretical predictions. Beside preliminary results by ourselves [18], no experimental approach has been published that directly enables simultaneous measurement of all substantial contributions to the total energy release rate directly from macroscopic properties without assuming specific electrical boundary conditions of the crack.

Against this background, a four-point-bending experiment with poled PZT specimen is performed under mechanical loads and applied electric fields from −500 to +500 V/mm, i.e., anti-parallel and parallel to the poling direction, respectively. As will be described in Sec. 3, the experimental setup used enables simultaneous in situ determination of the three linear components of the total energy release rate, i.e., the mechanical, the electric, and the piezoelectric part, as a function of the crack length and for differ-

[1]Currently at Robert Bosch GmbH, Corporate Sector Research and Aerospace Engineering, Postfach 106050, D-70049 Stuttgart, Germany.

Contributed by the Applied Mechanics Division of ASME for publication in the JOURNAL OF APPLIED MECHANICS. Manuscript received April 15, 2004; final manuscript received March 19, 2007. Review conducted by Robert M. McMeeking.

ent applied electric fields. Concerning the mechanical energies, the linear elastic and nonlinear contributions to the energy release rate were separated experimentally.

2 Theoretical Basis

In the following, the theoretical framework used to determine the energy release rate and the toughness is described. We apply Griffith's energy balance to our PZT material, which is ferroelectric and ferroelastic. This means that if a combination of stress and electric field is inside the switching surface, the material behaves completely linearly piezoelectric. If the electric field and mechanical stress are outside this region, domain switching takes place that leads to a change of the remanent polarization and remanent strain in these volumes. As will be seen in the following, it is not necessary for this investigation to know the switching criteria and constitutive equations in order to evaluate the energy changes in the PZT ceramic. We mainly use the experimentally determined linear part of the potential energy Π [3]:

$$d\Pi = -\Delta dF - Q dV - \mathcal{G} dA \tag{1}$$

Here, A is the crack surface area and Δ, F, Q, and V are displacement, force, charge, and voltage, respectively. In the following "linear part of the energy" or "linear energy release rate," respectively, means that the energy contributions, being partly quadratic in F or V, are attributed to the "linear" part of the constitutive equations. Equation (1) defines $\mathcal{G}$ as the crack driving force or energy release rate. Since the investigated PZT ceramic is ferroelectric and ferroelastic, the displacement Δ has a linear elastic part Δ_l and a remanent part Δ_r coming from the ferroelastic state and including inelastic as well as residual elastic deformation:

$$\Delta = \Delta_l + \Delta_r \tag{2}$$

Similarly, we have linear dielectric behavior leading to charges Q_l and remanent polarizations leading to charges Q_r:

$$Q = Q_l + Q_r \tag{3}$$

By using the linear terms of Eqs. (2) and (3), we get the linear part of $d\Pi$:

$$d\Pi_l = -\Delta_l dF - Q_l dV - \mathcal{G}_l dA \tag{4}$$

In the case of stable steady state crack growth, a fracture criterion can be formulated, where $\mathcal{G}_l$ reaches the critical value $\mathcal{G}_{lc}$. (The subscript "c" means "critical.") Sakai and Bradt [19] gave different methods for separating the energies due to linear and nonlinear processes during crack advance. We use one of them to evaluate our experimental data. They also stated that the change in energy due to linear processes during crack advance can be associated with the breaking of the atomic bonds, meaning the intrinsic part $\mathcal{G}_c^{\text{intr}}$ of the toughness. Using this assumption and generalizing it tentatively on the piezoelectric case, we obtain directly from Eq. (4) with F and V being constant:

$$\mathcal{G}_c^{\text{intr}} = \mathcal{G}_{lc} = 2\gamma_s = -\left(\frac{\partial \Pi_l}{\partial A}\right)_{F,V}^{c} \tag{5}$$

with γ_s being the effective surface energy. Strictly speaking, the assumption that the linear processes correspond to the intrinsic toughness has not been proven, but it seems reasonable and therefore it is used here. The domain switching area also contains elastic residual stresses, which can influence the intrinsic energy release rate; these stresses, in principle, would not be measured with our compliance method, described below. On the other hand, the specimen compliance is dependent only on the crack length (assuming a constant elastic modulus, see further below) and is not dependent on how much the crack advance is influenced by residual stresses. The energy from residual stresses would be newly created during crack growth. The difference between this created energy and the amount contributing to crack advance remains as residual stress energy in the crack wake. It contributes to the overall toughness and would be constant along the crack in the case of steady state crack growth. Thus, it is necessary to assume steady state conditions. This issue has been addressed before by Rose and Swain [20].

In the process zone, the remanent polarization and the remanent strain change because of the high stress and electric field. Thus, beside $\mathcal{G}_c^{\text{intr}}$, other processes exist, connected with domain switching, and leading to a toughness increase $\Delta\mathcal{G}_c$ as well as to a heightened overall toughness $\mathcal{G}_c$. Crack propagation takes place if the total energy release rate $\mathcal{G}$ becomes equal to a critical value, i.e., $\mathcal{G}=\mathcal{G}_c$, with

$$\mathcal{G}_c = \mathcal{G}_c^{\text{intr}} + \Delta\mathcal{G}_c \tag{6}$$

Here the term $\Delta\mathcal{G}_c$ is not further specified. A detailed description of the segmentation into different energy contributions for the presence of a switching zone in ferroelectrics is given by Kreher [21].

The linear part of Π in Eq. (1) can be expressed with the compliances for linear piezoelectric materials as proposed by Suo [22]:

$$\Pi_l(V,F,A) = -\frac{1}{2}C_e^F V^2 - \frac{1}{2}C_m^V F^2 - C_p VF \tag{7}$$

where C_e^F, C_m^V, and C_p are the electric capacitance, the mechanical compliance, and the piezoelectric compliance, respectively. The superscript "F" means constant force and "V" means constant voltage. The electric charge Q_l and the displacement Δ_l are given by

$$Q_l = (-\partial\Pi_l/\partial V)_{A,F} = C_e^F V + C_p F \tag{8}$$

$$\Delta_l = (-\partial\Pi_l/\partial F)_{A,V} = C_m^V F + C_p V \tag{9}$$

The energy release rate due to the linear processes therefore is

$$G_l^{\text{tot}} = -\left(\frac{\partial \Pi_l}{\partial A}\right)_{F,V} = G_e^F + G_m^V + G_p \tag{10}$$

where

$$G_e^F = \frac{V^2}{2}\frac{\partial C_e^F}{\partial A} \tag{11}$$

$$G_m^V = \frac{F^2}{2}\frac{\partial C_m^V}{\partial A} \tag{12}$$

and

$$G_p = FV\frac{\partial C_p}{\partial A} \tag{13}$$

are the linear electric, mechanical, and piezoelectric components of the energy release rate, respectively. From Eqs. (8) and (9) we readily find:

$$C_e^F = \left(\frac{\partial Q_l}{\partial V}\right)_{A,F} \tag{14}$$

$$C_m^V = \left(\frac{\partial \Delta_l}{\partial F}\right)_{A,V} \tag{15}$$

and

$$C_p = \left(\frac{\partial Q_l}{\partial F}\right)_{A,V} = \left(\frac{\partial \Delta_l}{\partial V}\right)_{A,F} \tag{16}$$

Since $C_p^F = C_p^V$ and therefore $G_p^F = G_p^V$, the superscripts of C_p and G_p are omitted. In order to determine the linear contributions to the total energy release rate, C_e^F, C_m^V, and C_p must be measured for different crack lengths. This enables calculating the derivatives of the compliances with respect to the crack surface area. Hence, the

experiment must be performed under conditions of stable crack growth.

We are aware of the fact that the quantities G_e, G_m, and G_p are not invariant to the transformation of the variables, as e.g., a change from the variables F and V to the variables F and Q. But although the different energy parts vary quantitatively, the sum of the components, which is $\mathcal{G}_c^{\text{intr}}$ at crack growth, remains the same. It is mentioned here that in the literature, as for example by Park and Sun [8], the linear release rate from the closure integral is decomposed into a mechanical and an electrical part, representing an invariant formulation. On the other hand, we use Eqs. (11) to (13) because the given energy components can be measured best in this composition. Thus e.g., the mechanical part G_m^V in this paper differs from G_m in Ref. [8]. (The only exception is at zero electric field, since then we have $G_m^V = G_l^{\text{tot}}$.) To avoid confusion, we add superscript "V," "F,"or "(Δ)" to the quantities to indicate the given boundary conditions.

For the correct data evaluation, the capacitance needs to be measured at constant force F, represented by C_e^F. In our experimental device, which is displacement controlled, the capacitance is measured at constant displacement Δ, denoted by C_e^Δ. From thermodynamic considerations, the following relation can be derived:

$$C_e^F = C_e^\Delta \left(1 + \frac{C_P^2}{C_e^\Delta C_m^V}\right) \tag{17}$$

Thus, we get C_e^F directly from the measured quantities. For our bending experiment in the range of crack lengths below 2.5 mm, the quotient in the brackets on the right-hand side of Eq. (17), a measure for the difference between C_e^Δ and C_e^F, is below 0.05%. However, the conversion is taken into account, because C_e^F can be calculated exactly.

In the following all energy release rates refer to the critical state of controlled crack growth. Thus, the superscript "c" for "critical" is not always given.

Since in our experiments the crack length is measured during controlled crack growth, the mechanical stress intensity factor K_I can be determined. In the Griffith crack solution, with the polarization vector acting perpendicular to the crack surface, K_I is independent of any external electric load [3]. Fully coupled piezoelectric finite element (FE) calculations for the given geometry, including combined electromechanical loading, also reveal that K_I is not dependent on the electric field [23]. The corresponding equation, taken from [23], is:

$$K_{\text{I}} = \sqrt{w}\sigma_a k_{I\sigma}(\alpha) \tag{18}$$

with $\sigma_a = (3/2)(F/b)(s_o - s_i)/w^2$ being the bending stress of an uncracked sample loaded by the force F; s_o and s_i are the outer and inner support distances, respectively, b the thickness, and w the height of the specimen. Concerning K_I, we get identical shape functions $k_{I\sigma}$ for the permeable and the impermeable crack:

$$k_{\text{I}\sigma} = \frac{\sqrt{\pi\alpha}}{(1-\alpha)^{3/2}}(1.07 - 1.89\alpha + 2.14\alpha^2 - 0.95\alpha^3) \tag{19}$$

Here, $\alpha = a/w$ is the normalized crack length with a being the absolute crack length. The formula is valid for $0.05 < \alpha < 0.95$. The shape function $k_{I\sigma}$, based on the FE calculations, is approximated by a least-squares fit [23]. We evaluate K_I during stable crack growth and denote it as K_{I}^C in order to distinguish it from the mechanical fracture toughness K_{IC}.

3 Experimental Procedure

3.1 Preparation of Specimens. Commercially available morphotropic PZT ceramic bars (PIC151, PI-Ceramic, Lederhose, Germany) of dimensions $3 \times 4 \times 28$ mm^3 are poled in the longitudinal direction using an electric field of 1.7 kV/mm (47.5 kV) for 15 min at room temperature. Before poling they were polished on the long side to enable microscopic determination of the crack extension. After poling the notch is cut with a diamond saw blade of 120 μm thickness and sharpened with a razor blade as specified by the single edge V-notch beam method (SEVNB) [24,25]. The notch depth is always about 1.0 mm and the tip radius around 10 μm.

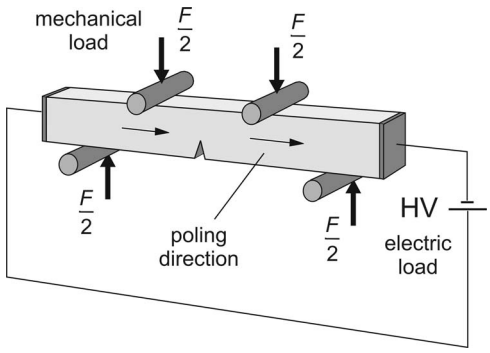

Fig. 1 Schematic geometrical four-point-bending setup with electromechanical load

3.2 Experimental Setup. Fracture experiments are performed under conditions of stable crack growth in a four-point-bending device. The supports used (Fraunhofer-Institut für Werkstoffmechanik, Freiburg, Germany) have support distances of 10 mm and 20 mm and a roller diameter of 5 mm. Ceramic rollers are used to achieve electrical insulation. The principal experimental setup is given in Fig. 1.

The supports are mounted in a very rigid metal frame (Fig. 2) as similarly done before by Fett et al. [26]. The dead weight of the upper support is compensated by weights connected via a rotatable wheel, which is dynamically decoupled using a spring. A steel plate is pre-stressed in the frame to reduce the thread slackness of the main screw (1) (Fig. 2), and thus increases the stiffness of the device. The displacement at the load points on the sample is changed manually using a hand wheel and a helical gear unit (E040B, ZAE Antriebs Systeme, Hamburg, Germany). This allows a precise and instantaneous control of the displacement with the precision of a few nanometers. The load accuracy is around 0.01 N. Due to its high stiffness, a quartz sensor (quartz dynamic load cell 9212, Kistler Instrumente GmbH) of high sensitivity (−11.3 pC/N) is used to measure the force. Quartz sensors exhibit an electrical drift, which must be taken into account. Since the overall drift is linear, this effect can be compensated.

The compliances are determined by a small modulation of the displacement. Therefore, a thin piezo-actuator is placed in the load line and excited by a low ac voltage of 5 Hz frequency. Simultaneously, the displacement of the upper supports with a modulation amplitude of about 30 nm is measured using an inductive position encoder (Fig. 2). In order to apply the theory correctly, the displacement is measured at the points where the mechanical load is induced. This is at the upper support rollers, from where the displacement is transferred via a movable linkage to the position encoder. In addition, we assume that the small displacement amplitude of 30 nm only leads to a linear response of the PZT sample, which is substantiated further below. It means that we measure $\mathrm{d}\Delta_l$ and $\mathrm{d}Q_l$ for different crack lengths (but each measurement at constant crack length).

Optionally, the specimen can be loaded with high voltage up to 14 kV, i.e., an electric field up to 500 V/mm. In parallel, the capacitance and the electric current are measured using custom-made electronics (schematic diagram in [27]). The capacitance measurement has been calibrated with different capacitors, previously characterized with a precision LCR meter (Hewlett-Packard 4284A). Thus, an accuracy of about ±0.02 pF is determined for

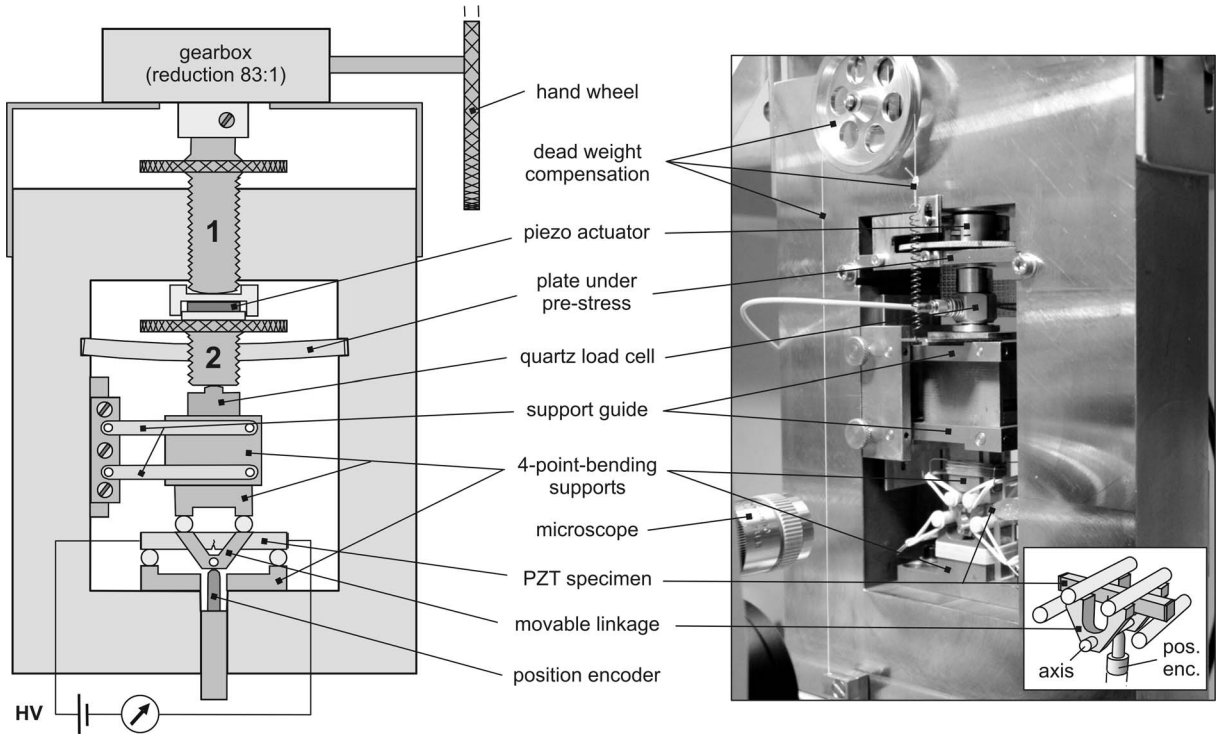

Fig. 2 Schematic drawing and photograph of the displacement controlled four-point-bending device. The insertion in the photograph shows the mechanical arrangement to measure the displacement of the upper support. The two V-shaped rods are movably connected by an axis and transfer the displacement of the upper support rollers to the position encoder. The electrical insulation at the high voltage side of the specimen is achieved by a coating with thermoplastics.

the measurement of capacitance changes. The ac signal (10 kHz, amplitude 1.5 V) necessary for this purpose is negligible compared to the applied electrical load of several kV.

According to Eq. (16), two equivalent procedures are possible to access the piezoelectric compliance. Varying the mechanical load under constant voltage, the change of the charge in the sample can be determined, i.e., $C_p^V=(\partial Q_l/\partial F)_{A,V}$. Another method is to alternate the voltage under constant force, which yields a change of the displacement, i.e., $C_p^F=(\partial \Delta_l/\partial V)_{A,F}$. Since the high voltage is kept constant by the power supply, the first option can be realized directly with the modulation technique and is used for all measurements presented in this paper. The second option was implemented only for test purposes. Generally, during the measurement of C_e^F, C_m^V, and C_p, the crack length remains unchanged.

For the evaluation of the compliances from the modulated mechanical load, the amplitudes of the force (dF), the linear displacement ($d\Delta_l$), and the electric current (dI) must be correlated. Therefore the signals are recorded using a PC with a built-in AD converter. The amplitudes are determined by fitting sine functions to the measured data containing ten periods, which means 2 s measuring time per data point. Actually, amplitude and phase are fitted, whereas the frequency of 5 Hz is fixed. The evaluation procedure is similar to the formalism used in lock-in techniques. The compliances are calculated afterwards according to Eqs. (15) and (16) using the amplitudes of the fitted functions. The charge dQ_l necessary to calculate the piezoelectric compliance is determined by analytical integration of the sine function, which corresponds to the current signal. The accuracy of the current signal is ±0.02 pA. Furthermore, K_I^C at crack growth is calculated according to Eqs. (18) and (19) using the applied load and the crack length measured with an optical microscope (Wild M3Z) (Fig. 2).

3.3 Measured and Derived Quantities. Since the experiment is relatively complex, the measured and derived quantities are listed in Table 1 as a basis for further analysis. The time t is needed for the linear drift correction concerning the quartz sensor. $\mathcal{G}_c^{\text{intr}}$ is derived solely from measured macroscopic quantities. The data are recorded simultaneously so that an entire set of parameters for all crack lengths is acquired with a single bending bar. As mentioned before, each measurement of dF, $d\Delta_l$, and dQ_l along crack advance is performed at constant crack length.

The measuring technique in combination with stable crack advance in piezo ceramics is quite new. Therefore, the main steps of the data evaluation, including the correction due to the finite compliance of the four-point-bending device, and due to the compression of the sample at the contact points are summarized in the Appendix.

Table 1 Measured and derived physical quantities. They are used in the equations given before and determined for every crack length. The numbers in brackets indicate the equations, which define the quantities. The amplitudes of the sine functions due to the tiny 5 Hz modulation are dF, $d\Delta_l$, and dQ_l, and lead to C_m^V and C_p. The energy release rate $\mathcal{G}_c^{\text{mech}}$ also includes remanent processes and is defined further in the text.

Measured	Calculated (Eq.)
F	C_m^V (15)
dF	C_p (16)
Δ	C_e^F (17)
$d\Delta_l$	K_I^C (18)
dQ_l	G_m^V (12)
V	G_p (13)
C_e^Δ	G_e^F (11)
a	$\mathcal{G}_c^{\text{intr}}$ (5) and (10)
t	$\mathcal{G}_c^{\text{mech}}$ (27)

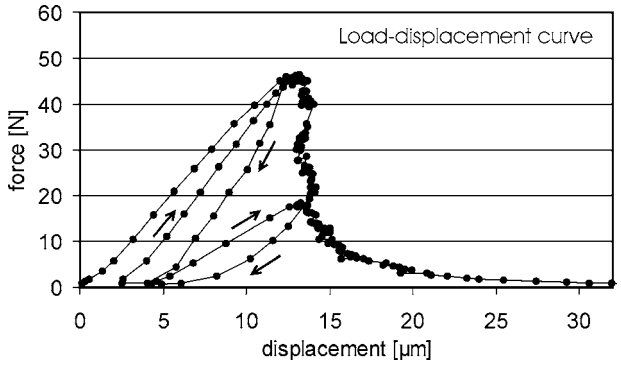

Fig. 3 Raw data of the load-displacement diagram for poled PZT. Two (out of six) unloading cycles are shown. The measurement is performed with the 5 Hz modulation.

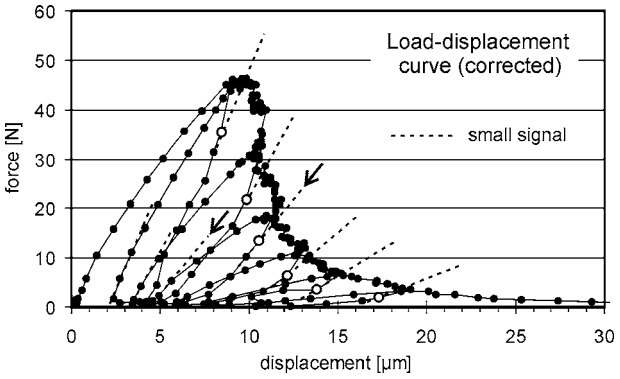

Fig. 4 Load-displacement curves of Fig. 3, including all six unloading cycles. The dotted "small signal" lines and the displacement are corrected according to Eqs. (A1) and (A5) in the Appendix . The starting point on the displacement axis is shifted arbitrarily to the origin (as also shown in Fig. 3).

4 Results and Discussion

4.1 Force-Displacement Curves and Their Interpretation. The raw data of a representative load-displacement curve of poled PZT without applied electric field (both electrodes of the specimen are connected with ground potential), including two unloading cycles, are given in Fig. 3. Already, the very first loading before crack growth leads to a remanent displacement of 2.5 μm after unloading. This effect is typical for all tests and for all applied electric fields. We interpret this inelastic behavior of the sample as the creation of a frontal process zone (see also Fig. 6). It can be seen that the unloading and the loading lines in Fig. 3 form closed hysteresis loops, implying that irreversible processes occur. The second unloading/loading cycle after substantial crack propagation of 1.5 mm shows the same irreversible hysteresis loop behavior. This is taken as switching of the ferroelastic domains around the crack tip during unloading and reloading. After a given crack advance of 1.5 mm and after complete unloading, an additional remanent displacement of about 1.5 μm is observed.

The areas of the "unloading hysteresis loops" become two to three times narrower if the 5 Hz modulation is not used. Obviously, the small mechanical modulation with an amplitude of 30 nm facilitates domain wall movements. But in both cases, i.e., with and without 5 Hz modulation, the inelastic remanent displacements as well as the slopes of the dashed loading lines, especially directly after reloading at $F=0$ N (arrows pointing up) are the same. In addition, the shape and the area of the main load-displacement curve are unchanged by the 5 Hz modulation.

The measured displacement in Fig. 3 must be corrected due to the device compliance and to the compression of the sample. For details, see the Appendix (Fig. 18 and Eq. (A5)). The corrected diagram of Fig. 3 is shown in Fig. 4 with all six unloading/loading cycles. The open circles in Fig. 4 represent the places of slight unloading, where the small signal compliance C_m^V is measured. The slopes of the dotted lines, corresponding to $1/C_m^V$, run nearly tangentially to the unloading lines.

The loading lines are slightly curved (Fig. 4), implying that the specimen becomes softer with increasing force. This seems reasonable because of increasing domain switching. On the other hand, the slopes of the small signal compliance values (dotted lines) fit well to the unloading/loading cycles when reloading starts at $F=0$ N. The two arrows in Fig. 4 indicate two parallel dotted lines representing the small signal compliance. Additionally, when measuring the small signal compliance along the data points of an unloading/loading cycle, its value is almost constant within approximately 5% (except at forces less than about 5 N). It follows that the small signal compliance is independent of actual load conditions. (Note that the modulation amplitude of about 30 nm for measuring C_m^V is less than the *thickness* of the dotted lines.)

As a consequence of these results, we assume that the measured mechanical small signal compliance C_m^V represents solely the linear mechanical response of the ceramic. It means that under small signal modulation, no domain switching occurs because of the tiny modulation amplitude and the short time constant (5 Hz). If we vary the small signal amplitude as well as the frequency of 5 Hz by a factor of 2, C_m^V is unchanged within the experimental uncertainty. With a variation of about 1% C_m^V represents a minimum constant compliance value, implying that we measure below a certain threshold, where no domain switching occurs any more. It seems that even in the general case of large scale yielding, the modulation technique measures solely the linear response of the system.

The energy contributions during complete unloading of the specimen and during crack advance are shown schematically in the load-displacement diagrams in Figs. 5(*i*) and 5(*ii*). Here, we address the pure mechanical case, which turns out to be reasonable, when the electrical influence is examined further below. At point (c) (Fig. 5(*i*)) the elastically stored energy is given by the area (B). When unloading the sample completely from point (c) to (d), the area (C) denotes the energy, which is regained mechanically by domain back-switching. If loading again the specimen to point (c), the area (D) is a measure for the hysteresis energy, converted into thermal motion. The parallel lines 1 and 3 denote the (inverse) small signal compliance, corresponding to the linear elastic material response.

During the experiments for the evaluation of the critical energy release rates, the specimens were never unloaded, in order not to disturb the measurement. However, due to the small signal modulation technique, the total energy release rate can be separated into the energy due to linear elastic processes (area (E)) and the remanent energy (area (F)) as proposed by Sakai and Bradt [19] (see Fig. 5(*ii*)). Referring to that reference, we assume also that area (E) corresponds solely to the creation of a new crack surface. Area (F) includes energies from remanent inelastic processes as well as energies due to elastic residual stresses in the domain switching area, which influence the crack advance. Rose and Swain [20] denote the overall energy (E)+(F) per newly created crack surface as specific incremental "work of fracture." Note that the displacement increment $d\Delta_l$ in Fig. 5(*ii*) due to linear processes at crack advance is not identical to the quantity $d\Delta_l$ in Table 1, which is measured at constant crack length. The two quantities ($d\Delta_l$ and $d\Delta_r$), given in Fig. 5(*ii*), are not used further in this paper and are given only for clarification with respect to Δ_l and Δ_r in Eq. (2).

The hysteresis processes during unloading and loading can be explained by a process zone, which is partly reducing its size during unloading and is increasing again during loading. In Fig. 6,

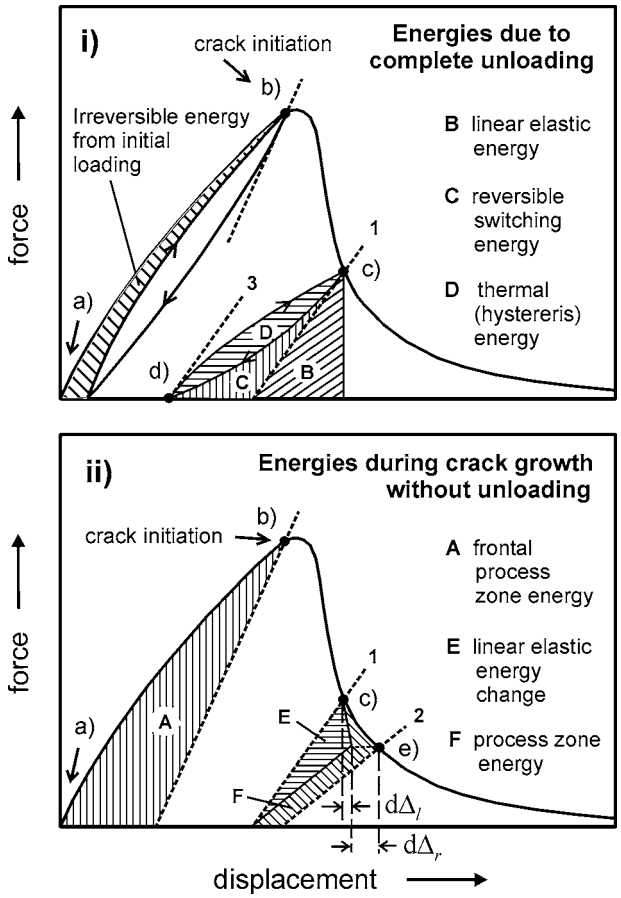

Fig. 5 Schematic load-displacement diagrams for crack advance in ferroelectric PZT. (i) Energies during a complete unloading cycle at crack initiation and after a certain crack advance, (ii) energies during crack growth from (c) to (e) without unloading.

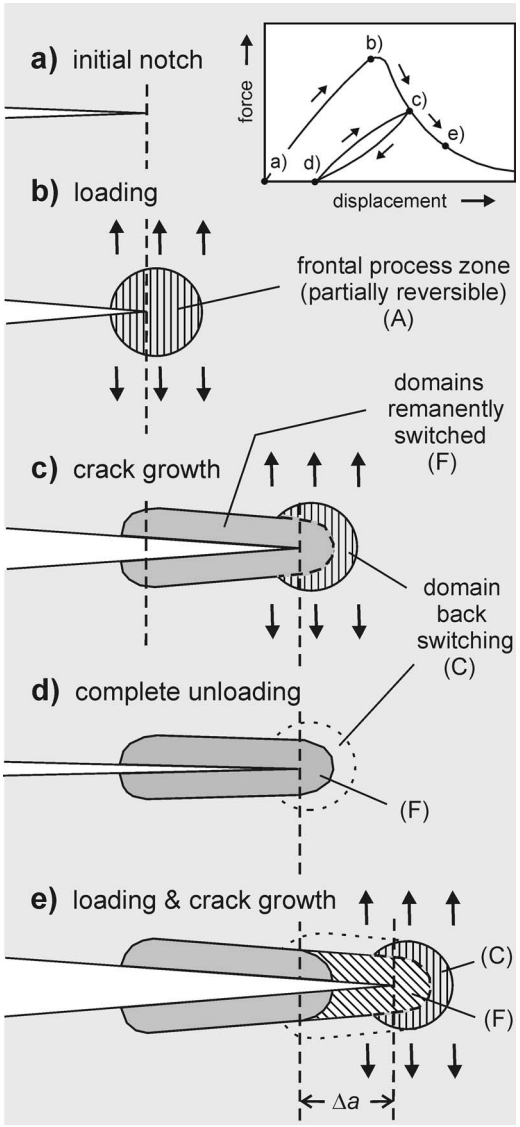

Fig. 6 Schematic crack and process zone area. (*a*) Initial notch. (*b*) The specimen is loaded to a value just before the crack starts to grow, which creates the frontal process zone. (*c*) The crack has grown. (*d*) The specimen is completely unloaded. (*e*) The crack is loaded again and has grown by an amount Δa. The diagonally hatched area (F) in (*e*) shows the process zone area of remanently switched domains, corresponding to the crack extension Δa. The vertical arrows indicate tensile stress. The capital letters (A), (C), and (F) correlate to the corresponding areas in Fig. 5. The panels (*a*) to (*e*) correspond to the points (a) to (e) in Fig. 5.

the crack and the process zone are shown schematically. The charts 6(*a*) to 6(*e*) in Fig. 6 correspond to the points (a) to (e) in the inset force-displacement diagram and to Fig. 5. The very first loading from (a) to (b) in Fig. 5(*i*) shows some nonlinearity that we interpret as the creation of a frontal process zone. By unloading the sample from points (c) to (d) (Fig. 5(*i*)), the process zone around the crack tip decreases by the vertically hatched area (C) in Fig. 6(*c*). Reloading from points (d) to (c) increases the process zone again and leads to the nonlinear load-displacement curve. Therefore, the process zone height in the crack wake is drawn smaller than the process zone at the crack tip. Due to this reversible process, we assume partial domain back-switching in the wake. When the crack grows by an increment Δa from (c) to (e) (Figs. 5(*ii*), 6), the fully developed process zone is shifted under stationary conditions along the distance Δa. The diagonally hatched area (F) in Fig. 6(*e*) indicates the area of remanent domain switching belonging to Δa (energy (F) in Fig. 5(*ii*)).

With this interpretation of the load-displacement curve at zero electric field, the intrinsic toughness during stable steady state crack growth as defined in Eq. (5) is

$$\mathcal{G}_c^{\text{intr}} = G_m^V = \frac{\text{area(E)}}{\Delta A} \tag{20}$$

The toughness part, including domain switching, during steady state crack growth is

$$\Delta\mathcal{G}_c = \frac{\text{area}(F)}{\Delta A} \tag{21}$$

The interpretation of the force-displacement curve given above is also applied for mechanical loadings with a constant applied electric field. Under constant voltage, the F-Δ curve includes the piezoelectric displacement Δ_p, which can be calculated according to $d\Delta_p = V dC_p$. The compliance $C_p(A)$ is a function of the crack length and the measured value varies roughly between ±10 pm/V for the essential crack extensions (see Figs. 8(*b*) and 9(*b*)). Accordingly, for maximum applied voltages of 14 kV, the piezoelectric displacement varies between ±0.14 μm, which is small enough to be neglected.

Since the Q-V curve during crack extension is not measured,

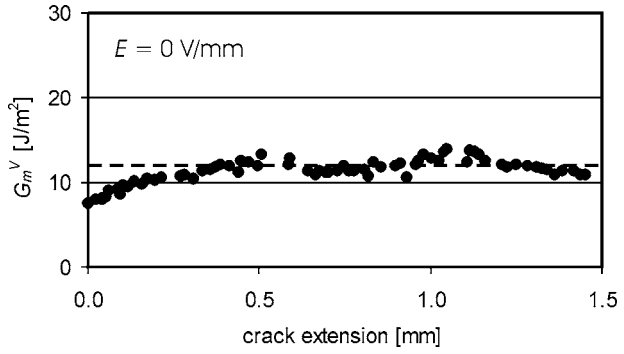

Fig. 7 Intrinsic toughness for poled PZT without applied electric field. The compliance curve for calculating the energy release rate is fitted for crack extensions between 0 mm and 1.5 mm. The dashed line represents 12 J/m².

we only have information about the mechanical remanent energy part. With our experimental setup, it was not possible to determine the total $\Delta\mathcal{G}_c$, because we do not know the whole electrical energy change due to irreversible processes. (A rough estimate is given further below.) On the other hand, we have the complete information to calculate $\mathcal{G}_c^{\text{intr}}$ by evaluating the compliances C_e^F, C_m^V, and C_p during stable crack growth and entering them into Eq. (10).

4.2 Critical Energy Release Rate. As the small signal modulation measures the linear elastic response, we may apply the approach of Suo using Eqs. (10) to (13). For zero electric field, the resulting intrinsic toughness $\mathcal{G}_c^{\text{intr}}=G_m^V(a)$, given in Fig. 7, is approximately 12 J/m^2.

With the setup in Fig. 1, the electric loads between −14 kV and 14 kV had been applied before the specimens were loaded mechanically. Furthermore, for all electric loads including zero field, the specimens were not unloaded in between, as said before.

As expected, the measured mechanical compliance C_m^V at electric fields of −500, −250, 0, 250, and 500 V/mm reveals a monotonic increase with respect to the crack length (Fig. 8(*a*)). The curves look similar, irrespective of the applied electric field. The piezoelectric compliance curves in Fig. 8(*b*) are also similar except one at −500 V/mm, which proceeds significantly higher than the other curves. The strong electric field opposite to the poling direction together with the high mechanical stress probably leads to large scale domain reorientation processes. Although the applied field is definitely below the coercive field of approximately E_c=850 V/mm, it is probable that the original piezoelectric state of the PZT ceramic is already disturbed.

The calibration of the current and charge measurement, respectively, was verified in a uniaxial compression test with a cubic poled PZT PIC151 specimen. The zero crossing of C_p can be understood qualitatively as follows. For an ideal bending bar, in principle, the piezoelectric compliance is zero. The charges generated in the compression and in the tension zone compensate each other. In the present case, the bending bar is single edge notched, which leads to asymmetric behavior. This asymmetry probably changes its characteristic, as the crack proceeds through the specimen, which could explain the tendency in Fig. 8(*b*). Both quantities C_m^V and C_p are corrected according to Eqs. (A1) and (A2).

The electrical capacitance is not measured absolutely, but only its change is acquired with the precision mentioned above. Hence, the curves shown in Fig. 8(*c*) are shifted vertically to fit the arbitrarily chosen mutual value of 8.5 pF at a crack length of a =1.5 mm. (It is a typical capacitance of the used specimens with such crack length.) For crack lengths smaller than 3 mm, the capacitance curve is nearly linear and for longer cracks, it declines strongly.

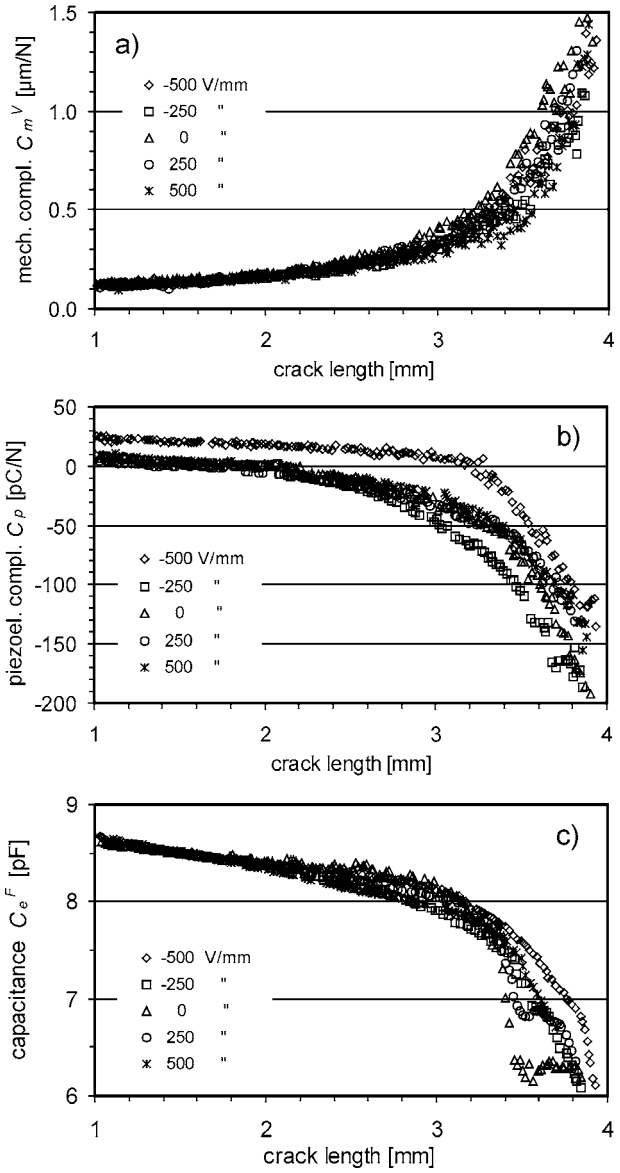

Fig. 8 (*a*) Mechanical and (*b*) piezoelectric compliance as well as (*c*) capacitance as a function of the crack length for different electric fields and corrected according to Eqs. (A1) and (A2). For a better comparison the crack length is used, being the sum of notch depth (between 0.98 mm and 1.07 mm) and crack extension.

For calculating the derivatives of the compliances, suitable analytical functions are fitted with respect to the crack length. The functions and the motivation for their choice are given in the Appendix (Eqs. (A6) to (A8)). Figure 9 presents the curves for E=500 V/mm. The quantities are fitted between 0 mm and 1.8 mm crack extension corresponding to 1.0 mm and 2.8 mm of total crack length.

Note that the piezoelectric compliance $(\partial Q_l/\partial F)$ in Figs. 8(*b*) and 9(*b*) exhibits an unsteady behavior like a step at the zerocrossing. With increasing crack length, the decreasing charge amplitude dQ_l as a function of time (sine function) does not continuously pass zero, which would be equivalent to a sudden phase shift of 180 deg. Instead, the charge amplitude dQ_l passes a minimum at a small positive value, and simultaneously the phase is shifted slowly from 0 deg to 180 deg. Since, in the calculation of C_p (Eq. (16)), this continuous phase shift of the charge signal with respect to the force signal is not included, the sign of C_p is changed when

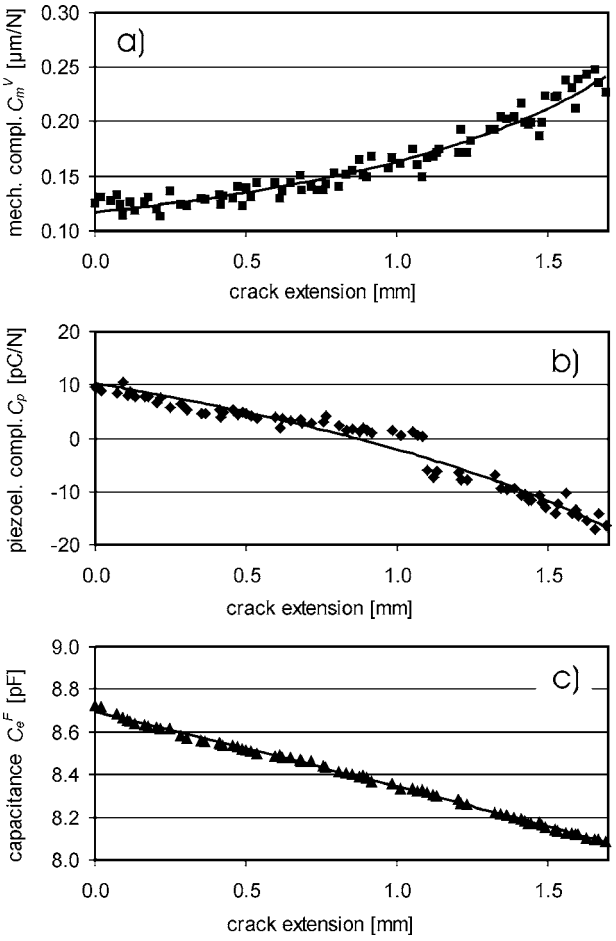

Fig. 9 (*a*) and (*b*) Compliances and (*c*) capacitance as a function of the crack extension for an electric field of 500 V/mm and corrected as described before. The fitted analytical functions are used to differentiate the experimental data with respect to the crack surface area. (For the discontinuity of C_p, see text and compare with Fig. 8(*b*)).

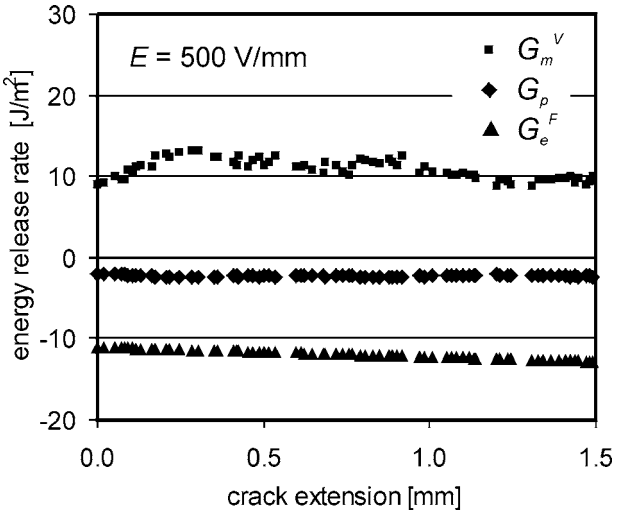

Fig. 10 Measured energy release rates G_m^V, G_e^F, and G_p for an electric field of 500 V/mm during stable crack advance

the measured phase shift becomes more than 90 deg. Thus, this drop of a few pC/N has a technical reason. It cannot be considered by the given theoretical approach and is bypassed, while fitting a smooth curve along this step in the C_p diagram. Fixing the phase at a certain value would yield a smooth zero crossing of C_p, but yields other difficulties while calculating C_p. In Fig. 8(*b*), it can be seen that this step is comparatively small with regard to the whole C_p curve.

The derivatives of the fitted compliance and capacitance curves are calculated analytically and multiplied by the measured force F and electrical load V according to Eqs. (11) to (13). Thus, for the linear processes we obtain the mechanical, the piezoelectric, and the electric energy release rates, which are shown in Fig. 10 for an electric field of +500 V/mm.

The evaluation of the mechanical energy release rate G_m^V during the first 200 μm crack extension that shows an increase with increasing crack length has a strong uncertainty. It stems from the increase of the force F at the beginning during the first 200 μm crack advance. Looking at the expression of G_m^V (Eq. (12)), the initial increase of the term F^2 can, in principle, be compensated by a corresponding variation of $\partial C_m^V/\partial A$. Nevertheless, $C_m^V(a)$ is fitted by a hyperbola of only three free parameters (Eq. (A6)), which does not allow us to fit short range variations.

The electric and the piezoelectric components are negative. For crack extensions from 0.5 mm to 1.5 mm, G_m^V, G_e^F, and G_p are almost constant as for all other applied electric loads. This indicates that the crack extension is in a steady state regime, which confirms the assumptions for the formulation of $\mathcal{G}_c$. At crack extensions above 2 mm, i.e., at crack lengths larger than 3 mm, the mechanical and the piezoelectric energy release rates approach zero smoothly. The electric part in that region, on the other hand, decreases dramatically down to about -150 J/m^2. We assume that at these large crack lengths the process zone touches the specimen's "back side." Additionally, the correction of C_m^V according to Eq. (A1) gets a strong influence on the result, since the device compliance C_{m01} is relatively large for small loads (compare Fig. 17(*a*)). Therefore, the range of crack lengths above 2.5 mm is not further analyzed.

Assuming a steady state crack growth between 0.5 mm and 1.5 mm crack extension, we average the data in this interval in order to minimize the experimental scatter and to display these medium values versus the applied electric field (Fig. 11).

Since the electrical field concentration at the crack tip is geometry dependent, it would be more appropriate to display the results as a function of the intensity factors K_I and K_IV. However, we would have to postulate certain boundary conditions in order to calculate an electrical intensity factor K_IV. Even if it has been experimentally shown that for the PZT used the apparent relative permittivity in the crack is not 1 but around 40 [14], the electric charge distribution on the crack surfaces is unknown. To avoid unproved conditions, we simply display the measured components of the energy release rate as a function of the (known) electric far field. The original notch depths are always within 0.98 mm and 1.07 mm and the other geometrical features are nearly identical for all specimens, so that the comparison in Fig. 11 is reasonable. The experimental data of the energy release rate contributions are presented without any theoretical assumption.

The measured energy release rate G_m^V at crack propagation is roughly constant over the measured range of applied electric fields. At zero electric field we have $G_m^V = 11.5$ J/m^2 (averaged for two samples). This agrees very well with the value of 12 J/m^2 found by Heyer et al. [28] for the same material but for a conducting crack at $K_E = 0$ kV/m$^{1/2}$, meaning pure mechanical loading.

The measured G_e^F values during controlled crack propagation are negative as expected [22] and exhibit a parabolic shape with respect to the electric load. The reason is as follows. As shown in Figs. 8(*c*) and 9(*c*), C_e^F and thus also $\partial C_e^F/\partial a$ are almost independent of the applied electric field. Hence, the part of the energy release rate given in Eq. (11) depends mainly on the square of the

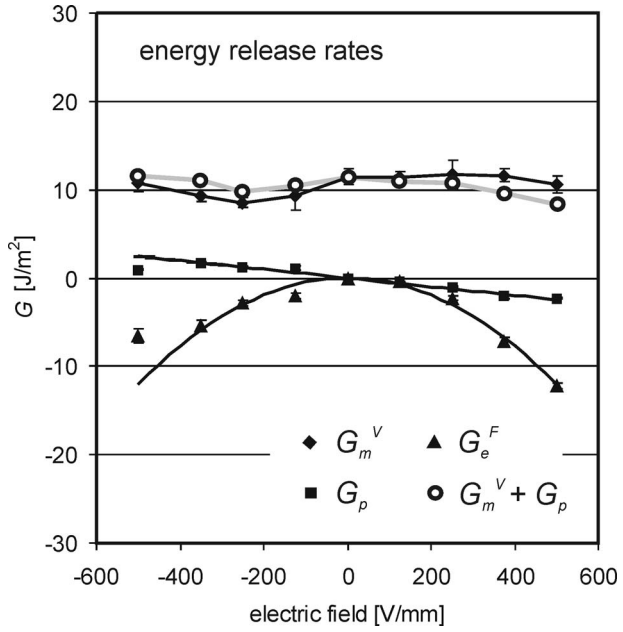

Fig. 11 Intrinsic energy release rates averaged between 0.5 mm and 1.5 mm crack extension. The linear and parabolic functions shown are valid for the idealized case, i.e., that the derivatives of C_p and C_e^F are independent of the electric field (see text). The data points are measured with only one sample for each electric field, except for the one at zero field, where two samples are averaged. The open circles connected by the gray line are the sum of all three contributions, where additionally G_e^F has been set to zero. Thus, actually it is the sum of G_m^V and G_p.

voltage V^2, which means that G_e^F is proportional to E^2 in this range of crack lengths. The piezoelectric part G_p during controlled crack propagation is small and shows a linear behavior, which can be explained by an analogous argument.

At applied fields of −500 V/mm, the piezoelectric and the electric energy release rates deviate from the main trend lines. We assume that this is due to the beginning large scale depolarization in the sample, as explained before in the context of Fig. 8(*b*).

Concerning the linear processes, Fig. 11 shows the three components of the total energy release rate available at crack growth. The sum of them, which we define as $\mathcal{G}_c^{\text{intr}}$ (Eq. (5)) or G_l^{tot} in the critical state (Eq. 10), respectively, is not constant, as we would expect. It even becomes negative for 500 V/mm. This is not compatible with the interpretation of $\mathcal{G}_c^{\text{intr}}$ as the energy necessary to break the atomic bonds. From the experimental results, it is appealing to take only the mechanical part G_m^V as the criterion for crack growth, because it is almost constant for all applied electric fields. A similar conclusion has already been suggested by Park and Sun [8], but the physical argument that justifies this approach is missing.

If we assume that free charges completely screen the remanent as well as the dielectrically induced polarization charges on the crack surfaces, the electric field would penetrate the crack cavity without any disturbance. As a consequence, there would not be any change in the measured capacitance as a function of crack length and G_e^F would be zero.

On the other hand, our measurements, which show a change in the small signal capacitance with crack length obviously contradict this assumption. A possible solution for this dilemma is that during the 10 kHz modulation of the voltage with an amplitude of 1.5 V biased by the high applied voltage of several kV, the screening charges cannot follow. The consequence is that the small signal modulation measurement (10 kHz) detects a purely linear response of our sample. Especially for the modulated signal and only for this, no screening charges are created at the crack surface. This would explain the measured change in capacitance with crack advance even though under the quasistatic conditions of crack growth, the polarization charges would be completely screened.

This explanation is in so far very probable because unscreened remanent polarization charges would lead to never measured extremely high crack growth retarding effects. This was shown theoretically in [16]. In almost all of the literature, it is implicitly assumed that the remanent polarization charges at the crack surfaces are screened. Taking this idea as serious, the induced polarization charges should also be screened, which is consistent with the above given approach. Sources for screening charges could be water surface layers or already existing ions, and produced ions and electrons from dielectric breakdown events in the crack cavity atmosphere.

A model assumption for breakdown in the interior of the crack is that the electric field cannot rise above a critical level. Thus, free charge is created and deposited on the crack faces sufficient to keep the electric field in the crack to the breakdown level [17]. As internal sources for screening, a small electric conductivity of the PZT could create space charges or domain switching localized at the crack surface and could average out the remanent polarization. A similar structure was detected during domain wall movement [29]. Both effects (screening and breakdown) would create an electric dc current during crack advance, which is not covered in the intrinsic energy release rate and would certainly influence the energy balance.

The measured change of the piezoelectric compliance is obtained by the slow 5 Hz modulation signal, which is applied mechanically. The charge response on the electrodes is due to the state of the sample with the assumed unchanged screening charges on the crack surface. Therefore, this electric signal should give the correct physical result.

For the evaluation of the linear energy release rate, we have to sum up the mechanical, piezoelectric, and electric part as given in Eq. (10), but now we set $G_e^F=0$, as explained above. The result for the total critical linear energy release rate with values between about 9 J/m^2 and 12 J/m^2 is shown in Fig. 11. This would imply that Eqs. (5) and (10) represent a theoretical approach, which practically must be modified in the case of electric loads, because then the physical situation is much more complex.

Although the resulting curve (open circles) is nearly constant, a slight dependency on the electric load seems to exist. Neglecting this dependency, we get an average value for G_m^V as well as for $G_m^V+G_p$ of about (10.5 ± 1.0) J/m^2. We assume that the small changes of up to 2 J/m^2 are significant and due to electric field effects of e.g., not completely screened polarization charges.

As far as we know, this is the first time that the intrinsic energy release rate was measured. In our opinion, care must be taken when comparing this result with other experiments such as those of Park and Sun [8], Fu and Zhang [12], or our own [23], which show different tendencies. In all the experiments performed before, it has not been distinguished between the linear part of the energy release rate and the energy release rate including domain switching effects.

4.3 Measured Fracture Resistance Curves at Different Applied Electric Fields. Even though the evaluation of the critical stress intensity factor during controlled crack growth is not the central issue of this article, it is easily possible to evaluate the measured crack growth data according to Eq. (18). The corresponding *R*-curves are shown in Fig. 12. These results must be treated carefully because they cannot be regarded as classical *R*-curves. The associated K_{IV}-curve would be needed additionally in order to give the full evaluation of the data which could be taken to identify a generalized mixed mode fracture criterion. (Therefore, the index "c" in K_{I}^c is written in the upper position.)

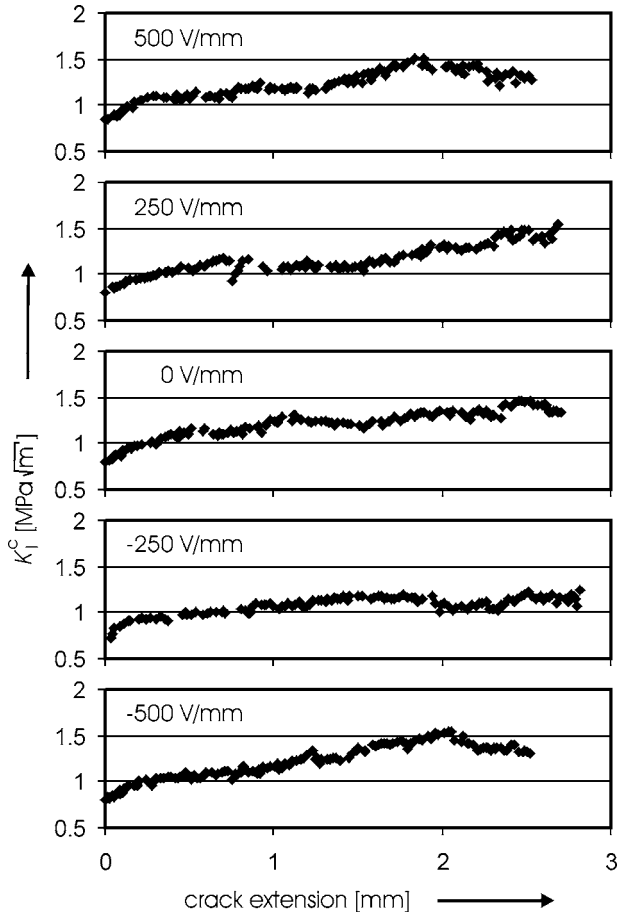

Fig. 12 Fracture resistance curves for external electric fields between –500 and 500 V/mm. The initial increase and also the main level are similar for all fields with the exception of –250 V/mm. Here, the curve proceeds slightly lower than the other ones.

Beside this it can be stated that under all applied electric fields, the fracture resistance curve is rising to a plateau value after about 0.3 mm crack advance.

From Fig. 12, we see that the *R*-curve at $E=-250$ V/mm proceeds significantly lower than the other curves, which is reflected by the tendency in Fig. 11. The corresponding mechanical energy release rate G_m is about 2 J/m^2 or 3 J/m^2 smaller than the values at the other electric fields. The slight unsteady increase of the *R*-curves differs from one to the other specimen, even at the same electric field. This is probably due to the individual crack path and residual stresses from poling in each specimen (more information is given further below).

4.4 Implications for the Stress Intensity Factor Applying Irwin's Equation. The crack closure integral leads to the Irwin matrix **H** (Suo et al. [3]), which establishes the link between the linear (crack tip) energy release rate and the crack tip stress intensity factor. The crack tip energy release rate is given by [3]

$$G_l^{\text{tip}} = \frac{1}{4}\mathbf{K}\cdot\mathbf{H}\cdot\mathbf{K}^T \tag{22}$$

with

$$\mathbf{K} = (K_{\text{II}}, K_{\text{I}}, K_{\text{III}}, K_{\text{IV}}) \tag{23}$$

and K_{I}, K_{II}, and K_{III} being the mechanical stress intensity factors and K_{IV} being the electric intensity factor at the crack tip. The symmetric Irwin matrix was calculated by Kemmer [30] for the material parameters of PZT PIC151 and since K_{II} and K_{III} are zero in four-point bending, we are left with

$$\begin{pmatrix} H_{22} & H_{24} \\ H_{42} & H_{44} \end{pmatrix} = \begin{pmatrix} 45.1\times10^{-12}\ \text{m}^2/\text{N} & 39.7\times10^{-3}\ \text{m}^2/\text{As} \\ 39.7\times10^{-3}\ \text{m}^2/\text{As} & -123\times10^{6}\ \text{V}^2/\text{N} \end{pmatrix} \tag{24}$$

Let $\Delta\varphi$ be the electric potential jump between the opposite crack faces. If we assume a permeable crack, then the condition $\Delta\varphi=0$ is equivalent to the following equation [3,23]:

$$K_{\text{IV}} = -\frac{H_{24}}{H_{44}}K_{\text{I}} \tag{25}$$

Inserting the expression of K_{IV} into Eq. (22) and using the quantities of Eq. (24), we get

$$\frac{K_{\text{I}}^2}{G_l^{\text{tip}}} = 4\left(H_{22} - \frac{H_{24}^2}{H_{44}}\right)^{-1} = 69\ \text{GPa} \tag{26}$$

During controlled crack growth, the crack tip energy release rate is physically this part of the released energy in the sample which is used to break the atomic bonds and therefore, in our terminology, the intrinsic toughness $\mathcal{G}_c^{\text{intr}}$. The experimentally measured plateau value of the intrinsic toughness for zero electric field is $\mathcal{G}_c^{\text{intr}}=G_m^V=11.5$ J/m^2.

The crack tip toughness is close to the starting value of the measured *R*-curves. Probably it is even a little bit less because already the frontal zone may lead to crack tip shielding. But since there is no other information available, we identify—as an attempt—the starting value of the *R*-curve with the intrinsic fracture toughness (without domain switching), being aware that this can be seen only as a rough estimate. For the measured K_{I}^C-curve without electric field (Fig. 12), we get $K^{\text{intr}}=0.82$ MPa$\sqrt{\text{m}}$ (averaged for two samples). Using the intrinsic toughness and intrinsic fracture toughness, we get $(K^{\text{intr}})^2/\mathcal{G}_c^{\text{intr}}=58$ GPa, which is in good agreement with the theoretical result of Eq. (26).

Furthermore, the FE calculations reveal that at zero electric field, K_{IV} for the permeable and impermeable crack are nearly the same within a few percent. Thus, if we assume the semipermeable crack being a "linear superposition" of permeable and impermeable crack [31], the above equations should be reasonable for all degrees of semipermeability.

4.5 Mechanical Inelastic Energies. Beside the intrinsic critical energy release rate $\mathcal{G}_c^{\text{intr}}$, we evaluate now the mechanical part of the total critical energy release rate $\mathcal{G}_c$ (Eq. (6)), including both intrinsic energies and all other remanent mechanical processes due to domain switching (area (E)+(F) in Fig. 5(*ii*)). This "energy release rate" $\mathcal{G}_c^{\text{mech}}$ is calculated from the load-displacement diagram as given by Sakai and Bradt [19]. Thus, we determine geometrically the area (E)+(F) (Fig. 5(*ii*)) and divide it by the corresponding new crack surface area dA. If we indicate the points (c) and (e) in Fig. 5(*ii*) with the indices "1" and "2" and taking into account that the slopes of the lines 1 and 2, are the inverse mechanical compliances $(1/C_m^V)$, we get:

$$\mathcal{G}_c^{\text{mech}} = \frac{C_{m1}^V F_1^2 + (F_1+F_2)(\Delta_2-\Delta_1) - C_{m2}^V F_2^2}{2\text{d}A} \tag{27}$$

According to Rose and Swain [20], this corresponds to the work of fracture, as said before. The equation cannot be applied directly to each pair of adjoining experimental data points because of the experimental scatter. Instead, we use an averaging procedure over several data points. In Eq. (27), F and Δ are averaged over each ten adjoining data points, C_m^V is taken from the analytical fit, and the result is averaged again as before. The work of fracture $\mathcal{G}_c^{\text{mech}}$, including the intrinsic toughness and also remanent processes, is given in Fig. 13 for applied electric fields of –500, 0, and

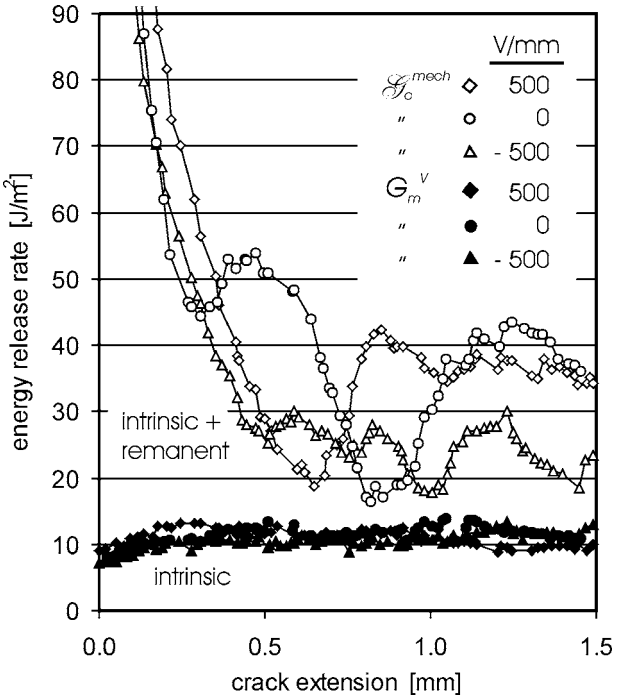

Fig. 13 Critical mechanical energy release rates, especially linear contribution (black points) and mechanical work of fracture (open points) for different applied electric fields (−500, 0, and +500 V/mm). The latter energy release rate comprises energies due to linear elastic processes as well as remanent energies.

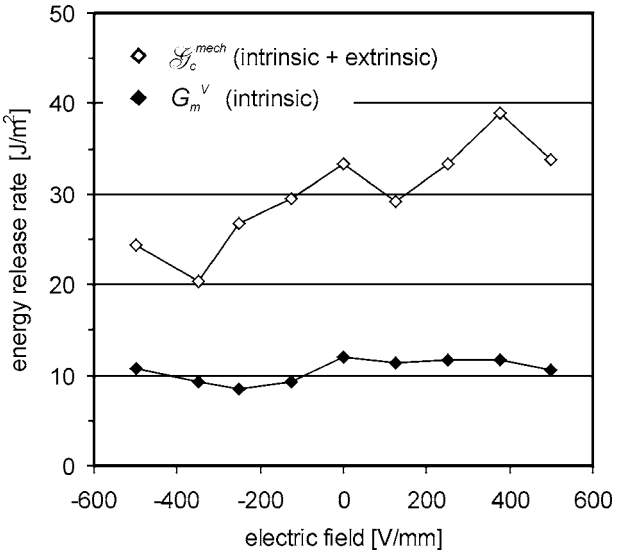

Fig. 14 Comparison of the "intrinsic" mechanical energy release rate G_m^V (lower curve, as in Fig. 11) with $\mathcal{G}_c^{mech}$ (upper curve) including remanent switching processes during crack advance. When calculating the standard deviation for the data points between 0.5 mm and 1.5 mm crack extension (Fig. 13), which gives a rough estimate for the error of the data, we get for the lower curve around ±1 J/mm² and for the upper curve about ±10 J/mm² (the latter number seems a little bit high.)

500 V/mm.

The high initial values of $\mathcal{G}_c^{mech}$ are based on energies from creating the frontal process zone. This effect was observed also by Rose and Swain [20] for partially stabilized zirconia. There are strong variations of $\mathcal{G}_c^{mech}$ for crack extensions above 0.5 mm, which are different for each specimen, even if the same electric field is applied. Thus, it seems that $\mathcal{G}_c^{mech}$ is quite sensitive on the individual crack path. This would include e.g., crack bifurcation, double cracks, and crack bridging. It means that these fluctuations are only qualitatively significant, but not their individual shapes. (Beside this we have to admit that the variations are possibly influenced by the evaluation procedure.)

On the other hand, the critical energy release rate G_m^V does not exhibit such variations, implying that the small signal compliance method is quite insensitive to the individual crack path, crack bridging, etc. For crack extensions above 0.5 mm, $\mathcal{G}_c^{mech}$ is about two to three times larger than $\mathcal{G}_c^{intr}$. Thus, in our four-point-bending configuration, remanent switching processes, being the difference $\mathcal{G}_c^{mech} - \mathcal{G}_c^{intr}$, are up to twice as large as $\mathcal{G}_c^{intr}$.

From Fig. 14, showing medium mechanical energy release rates (averaged between 0.5 mm and 1.5 mm crack extension) for different electric fields, we get the same result. For example, during the measurement at $E=375$ V/mm, much more crack branching and bridging was observed than in the other measurements, due to the properties of the individual specimen. This can be seen by the increased values in the upper curve (Fig. 14) at this particular electric field, but not in the lower curve for $\mathcal{G}_c^{intr}$. Looking at the general trend, the contribution to the energy release rate from remanent switching processes increases from −500 V/mm to 500 V/mm by about a factor of 2.

From load-displacement curves in which we unloaded the specimen completely just at the moment of crack initiation, we can evaluate the energy due to domain switching in the frontal zone. The energy stored is about $W_F=120$ μJ for our sample geometry (measured at zero external electric field).

There may be some concerns if so much energy is put only into the frontal zone or whether large scale deformation takes place. Kounga Njiwa et al. [32] used a liquid crystal display technique to monitor the electric surface potentials in front of the crack tip and estimated a switching zone size of 600 μm to 800 μm. Hackemann and Pfeiffer [33] applied a spatially focused X-ray diffraction technique and determined about 290 μm switching zone size. Both experiments were performed with PZT PIC151 and demonstrate a substantial switching zone. These experiments show that no large scale domain switching processes take place. A simple estimate confirms these experimental findings. If the remanent polarization of 0.32 C/m² [34] times 2 and multiplied by the coercive field of 0.85 kV/mm is taken as a measure for the energy density change during domain switching [35], we get about $w_s = 0.0005$ J/mm³. If we roughly approximate the frontal zone by a circle of area S going through the sample of thickness $t=3$ mm, S is calculated to be $S=W_F/w_S t$. For the linear dimension (diameter) of the switching zone size, this finally gives $2\sqrt{S/\pi} \approx 0.3$ mm, which corresponds well to the experimental results of [32,33].

In principle, the compliance change during crack extension is also affected by the growth of the process zone because the linear piezoelectric tensor is not isotropic. A polarization change may change the dielectric and elastic properties by approximately 10%. The volume change of an assumed remanent process zone of width 1 mm during a measurable crack extension dA of 50 μm $\times 3$ mm (sample thickness) is 0.15 mm³. Compared with the loaded sample volume of about 240 mm³, this leads to a negligible compliance change of less than 0.1%.

Thus, by evaluating the linear part of the energy release rate together with the load-displacement curve as described before, we can separate the linear (crack tip) energy release rate from switching zone processes. If in previous experiments these energy release rates were not separated, the detailed interpretation of the results sometimes seems difficult.

4.6 Electric Dissipative Energies. If $\mathcal{G}_c^{\text{elec}}$ is the electric energy release rate, including intrinsic as well as dissipative energies, we get for the toughness

$$\mathcal{G}_c = \mathcal{G}_c^{\text{mech}} + \mathcal{G}_c^{\text{elec}} \tag{28}$$

Whereas $\mathcal{G}_c^{\text{mech}}$ is determined from the load-displacement diagram using the measured mechanical compliance, the term $\mathcal{G}_c^{\text{elec}}$ can be derived in principle from a corresponding charge-voltage diagram using the measured capacitance.

A remark concerning the loading path must be added. The experiments with electric load are started by increasing the voltage up to a constant value before the sample is loaded mechanically. During crack growth, the voltage is kept at a fixed level by the power supply. With respect to the load-displacement diagram, an extension from the pure mechanical to the electromechanical case can be achieved, if we vary the electric load proportionally to the mechanical load. We would get a corresponding diagram with a generalized load and a generalized displacement. Unfortunately, in our case the situation is more complicated. On the other hand, the results show that the influence of the electric load is weak and therefore, we neglect this problem. The following should be seen as a rough estimate concerning nonlinear electrical processes.

As mentioned before, $\mathcal{G}_c^{\text{elec}}$ could not be measured, since the long-run charge measurement was disturbed by the capture of electromagnetic radio frequencies. Note that within the measured quantities in Table 1, only the charge modulation $\mathrm{d}Q_l$ is measured at constant crack length, whereas the accumulated charge Q during crack advance and in between is missing. Under electrical aspects, up to now we determined the state of the sample just before and after each crack advance.

In order to still get information about electrical processes during actual crack growth, the charge was measured during crack advance once with a poled PZT specimen at an electric field of 250 V/mm. Each crack advance takes about 1 or 2 s, so that electromagnetic disturbances during this time have only little influence. The electric current is automatically integrated during each measurement and divided afterwards by the area of the created new crack surface. The average charge generated immediately per new crack surface area was about $(410\pm200)\ \mu\mathrm{C/m^2}$ measured in the range of crack extensions between 0.5 mm and 1.5 mm. This phenomenon is clearly no piezoelectric effect, as could be seen in "short-time Q-F diagrams."

After stopping the crack the electric current does not stop immediately but decreases slowly. Such a delayed "time effect" in the behavior of PZT was observed on other occasions. However, it does not influence the measurement of the intrinsic toughness.

The measured charges ($410\ \mu\mathrm{C/m^2}$) if attributed to crack surface charges are less than 0.2% of the remanent polarization of $0.32\ \mathrm{C/m^2}$ for poled PZT PIC151. This is a strong indication that the remanent crack surface polarization charges are balanced by internal processes such as local domain switching or space charges. On the other hand, the dielectric polarization charge $P=\varepsilon_0\chi E$ for our material parameters gives about $2000\ \mu\mathrm{C/m^2}$, which is still higher than but much closer to the measured values. In summary, these results support the idea of screening crack surface charges or breakdown effects, but are not sufficient to demonstrate them, and additional, more refined measurements are necessary.

Concerning the total energy balance, a future experiment for measuring the total energy release rate including all electric dissipative processes is technically possible and might help to answer the remaining questions. However, beside this we hope that the present experimental data provide a useful basis for further discussions.

5 Summary

The intrinsic toughness as well as the extrinsic nonlinear domain switching toughening in polarized PZT PIC151 is measured. During stable crack growth, the mechanical and the piezoelectrical compliance as well as the electrical capacitance of the PZT sample is measured simultaneously as a function of the crack length using modulation/demodulation techniques. Computation of the derivatives of these generalized compliances with respect to the crack surface area allows for the calculation of the mechanical, the piezoelectric, and the electrical part of the energy release rate due to linear processes. To our knowledge, this is the first experimental result where these linear parts are well separated from nonlinear, especially domain switching contributions, although Rose and Swain [20] as well as Sakai and Bradt [19] had presented the basic principle before.

This novel experimental technique, based on the small signal modulation and stable crack growth, is easily applicable also to other ceramics with process zones in order to separate the intrinsic toughness from extrinsic nonlinear contributions.

With the assumption of screened polarization charges—for example due to electric breakdown—and by neglecting the slight electric field dependency, an average intrinsic toughness of $(10.5\pm1.0)\ \mathrm{J/m^2}$ for electric fields between -500 V/mm and 500 V/mm is determined. It seems probable that the slight field dependency of the measured intrinsic toughness is due to small contributions of the linear electric part of the energy release rate.

The information of the mechanical compliance and the load-displacement curve allows for the evaluation of mechanical energy changes related to domain switching in the vicinity of the crack. Additionally, a frontal process zone is identified. From the corresponding energy, a frontal zone size of the order of 0.3 mm can be estimated consistently to other experimental results. The mechanical toughening effect of the process zone is increasing from negative to positive external electric fields.

Acknowledgment

The support of this work by the German Research Foundation (DFG) is gratefully acknowledged. Furthermore, we thank T. Scholz as well as D. Schmidt from our group for their effective support regarding the realization of the experimental setup. We are indebted to C. Häusler from the Technical University Dresden for the idea of equal support distances in four-point bending, providing a method for the correct data preparation. We also thank P. Neumeister from the Technical University Dresden, as well as H. Keßler from Framatome ANP, Erlangen, and R. McMeeking from the University of California, Santa Barbara for valuable hints and discussions.

Appendix: Data Processing

Evaluation of C_m^V and C_p

The mechanical compliance is measured at constant voltage. To simplify matters, the superscript "V" is omitted. The finite compliance of the experimental device leads to corrections of the measured C_m and C_p values. The essential mechanical arrangement is given in Fig. 15, where $\mathrm{d}F$ and $\mathrm{d}\Delta$ are the measured 5 Hz modulation amplitudes of force and displacement, respectively. Thus, the measured mechanical (mm) compliance, simply, is $C_{mm}=\mathrm{d}\Delta/\mathrm{d}F$. To obtain the actual bending compliance of the specimen (C_m), C_{mm} must be decomposed according to Fig. 15.

Obviously, the compliance of the mechanical support of the specimen directly increases the overall compliance as described by the series connection. In addition, the specimen is compressed slightly by the support rollers. Both aspects are included in C_{m01}. Mainly because of the circular shape of the support rollers, C_{m01} is dependent on the applied load F. It is measured by using equal support distances of 20 mm each, as shown in Fig. 16(b). Taking the arrangements in Fig. 16, the subtraction (a)$-$(b) for each applied mechanical load F yields pure bending of the specimen. Concerning Fig. 15, the case in Fig. 16(b) means a parallel connection of C_{m01} and C_{m02} only.

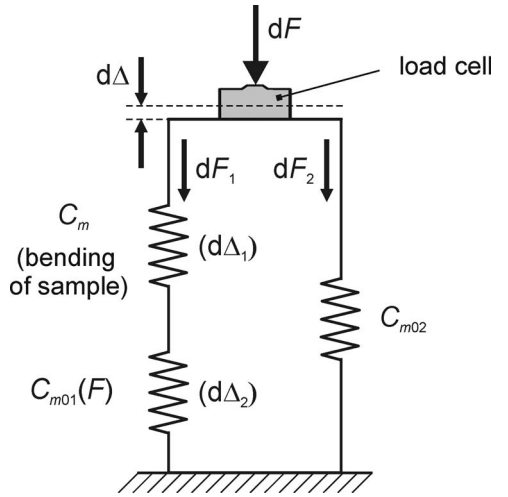

Fig. 15 Schematic arrangement of mechanical compliances of the specimen and the equipment with $C_{m01} \ll C_m \ll C_{m02}$. The parameters $d\Delta_1$ as well as $d\Delta_2$ are the displacements, belonging to C_m and C_{m01}. The latter one represents the compliance of the mechanical frame plus the compression compliance of the specimen and C_{m02} corresponds to small elastic deformations in the mounting and to inertia effects of the upper movable support.

Due to the dynamic modulation measurement, additional effects must be taken into account. Since the modulation amplitude is very small, frictional forces pin the rotatable wheel of the deadweight compensation (Fig. 2, right), which leads to a parallel connection of the decoupling spring. A similar effect could exist in the support guide. Together with the influence of the inertia of the slightly oscillating upper support mass, these effects can be summarized using an apparent compliance C_{m02} connected in parallel. This quantity can be determined directly by performing a measurement without a specimen, simulating an "infinite" specimen compliance. We get $C_{m02}=(16\pm2)\ \mu$m/N for both 10/20 and 20/20 mm supports. The compliance C_{m01} depends on the mechanical load F, whereas C_{m02} does not. Since the frequency of 5 Hz is much smaller than the resonance frequency of the oscillating mass, corresponding effects can be neglected.

With regard to Fig. 15 we have to consider at first C_{m02} for both arrangements (a) and (b) and then subtract the resulting compliances from each other. Thus, the pure bending compliance of the specimen is

$$C_m = \frac{C_{mm}}{(1 - C_{mm}/C_{m02})} - \frac{C_{m01}}{(1 - C_{m01}/C_{m02})} \tag{A1}$$

The correction of the piezoelectric compliance is similar. From the measured quantities using the 10/20 mm support we have $C_{pm} = dQ/dF$ and the analog value for the 20/20 mm support is C_{p01}. On the basis of Figs. 15 and 16 with $dF = dF_1 + dF_2$ and $d\Delta = d\Delta_1 + d\Delta_2$ (see Fig. 15) and replacing the displacements $d\Delta$, $d\Delta_1$, and $d\Delta_2$ by corresponding charge quantities, we obtain a similar expression for the piezoelectric compliance with respect to pure bending load:

$$C_p = \frac{C_{pm}}{(1 - C_{mm}/C_{m02})} - \frac{C_{p01}}{(1 - C_{m01}/C_{m02})} \tag{A2}$$

Note that a quantity C_{p02} does not exist, since without a specimen, no electric current can be measured. The denominators in Eqs. (A1) and (A2) are identical, correspondingly. The correction term C_{p01}, measured with the arrangement in Fig. 16(*b*), is slightly force dependent and of the order of 2 or 3 pC/N. The main difference between the mechanical and the piezoelectric case is that C_{m01} consists of *two* parts, i.e., the device compliance and the compression compliance of the sample, and that C_{p01} consists only of the piezoelectric compliance due to the compression of the sample. The associated corrections are approximately 5% to 30%, because mostly $C_{m01} \ll C_m \ll C_{m02}$ in the range of the analyzed crack lengths. To apply Eqs. (A1) and (A2), the compliances $C_{m01}(F)$ and $C_{p01}(F)$ are fitted by appropriate analytical functions (see Eqs. (A3) and (A4)). The corrected values of C_m and C_p are used in Eq. (17) for calculating C_e^F. The capacitance itself does not need any correction.

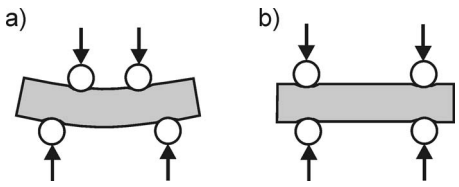

Fig. 16 Schematic drawing of the mechanical load configuration: (*a*) bending and compression of the specimen as well as loading of the device, (*b*) compression of the specimen and loading of the device. The difference (a)–(b) yields the pure bending compliance of the specimen.

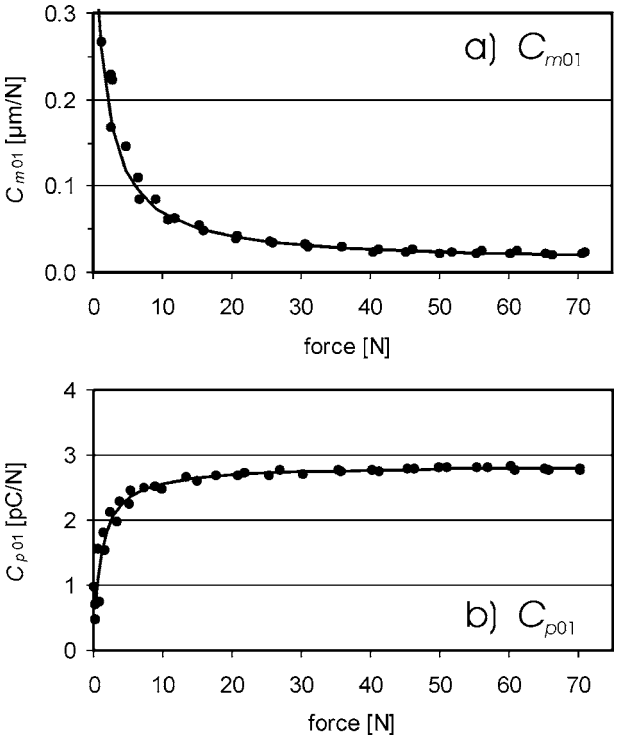

Fig. 17 (*a*) Mechanical and (*b*) piezoelectric compliance measured with the 20/20 mm supports (Fig. 16(*b*)).

The mechanical and the piezoelectric compliance C_{m01} and C_{p01} are given in Fig. 17 as a function of the applied mechanical load. At relevant forces of 10 N to 50 N, the mechanical correction term C_{m01} still decreases by a factor of 3 (Fig. 17(*a*)), whereas the piezoelectric term C_{p01} is almost constant around 2.7 pC/N (Fig. 17(*b*)). The latter value varies for different PZT samples by about ±10%. The functions fitted to the data are

$$C_{m01} = \left(\frac{0.6854}{F[\mathrm{N}] + 1.5896} + 0.01034 \right) \left[\frac{\mu\mathrm{m}}{\mathrm{N}} \right] \tag{A3}$$

and

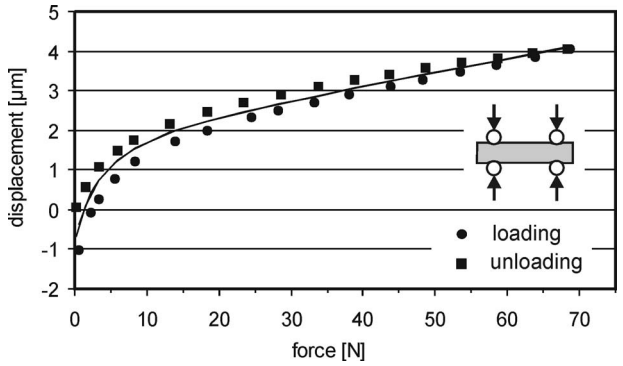

Fig. 18 Displacement as a function of the force, measured with equal support distances as in Fig. 16(*b*). As described before, this effect corresponds to the compliance of the mechanical support and to the compression of the sample. The zero position on the displacement axis is arbitrary. The slightly different paths for loading and unloading are fitted by the same curve (Eq. (A5)).

$$C_{p01} = \left(\frac{-3.1857}{F[\mathrm{N}] + 1.2039} + 2.8452 \right) \left[\frac{\mathrm{pC}}{\mathrm{N}} \right] \tag{A4}$$

Note that in Fig. 17, the compliance measurements are not dependent on whether the force increases or decreases. This emphasizes once more that the small signal compliance measurements are not influenced by the actual domain configuration and by switching processes.

Displacement Correction

The reasons leading to C_{m01} also yield an additional displacement, which has to be subtracted from the measured displacement. As before, this displacement is force dependent and determined directly by using the 20/20 mm supports. The data shown in Fig. 18 are fitted by the following analytical function:

$$\Delta_0(F) = \left(0.03399F[\mathrm{N}] + 1.800 - \frac{125.47}{(F[\mathrm{N}] + 7.00)^2} \right) [\mu\mathrm{m}] \tag{A5}$$

This function, describing the finite stiffness of the device and the compression of the sample, is subtracted from the measured displacement. The quantity C_{m02} originates from dynamical effects and therefore does not influence the quasistatic load-displacement measurement.

In principle, the data in Fig. 18 must be fitted separately for the loading and the unloading path. Nevertheless, this would make the data evaluation even more complicated. As this correction is relevant only for the load-displacement diagrams and not for the small signal modulation measurements, we use only the single curve in Fig. 18.

Analytical Functions Fitted to the Measured Compliances. The best results for the mechanical compliance are obtained using a hyperbolic function with $1/a$ characteristic, namely,

$$C_m(a) = \frac{p_1}{a - p_2} + p_3 \tag{A6}$$

where p_1, p_2, and p_3 are free parameters and a is the crack extension. For the fit of the piezoelectric compliance data, a logarithmic function is used:

$$C_p(a) = p_1 \ln\left(\frac{p_2 - a}{mm} \right) + p_3 \tag{A7}$$

and the capacitance is fitted by a second-order polynomial:

$$C_e(a) = p_1 a^2 + p_2 a + p_3 \tag{A8}$$

These functions are not chosen accidentally. In the case of using polynomial functions for C_m and C_p, the corresponding derivatives $\partial C_m/\partial a$ and $\partial C_p/\partial a$ and energy release rates exhibit strong variations depending on the order of the polynomial used, because the derivatives of C_m and C_p are rather small for short crack lengths. To avoid this, smoother functions should be used, which lead to more constant energy release rates. Generally, if we plot the applied force F as a function of the crack length, we obtain a nearly linear decrease with respect to the crack extension a. Hence, $\partial C_m/\partial a$ should have a $1/a^2$ characteristic to compensate the F^2 influence in Eq. (12). Integration of $\partial C_m/\partial a$ leads to the $1/a$ characteristic, which is finally used for C_m in Eq. (A6). The argument for C_p is analogous. For C_e^F, a polynomial of second order is sufficient. It is important that the choice of these functions has no physical intention. However, these functions require fewer free parameters than polynomials and fit very well to the experimental data.

The results are also sensitive to the range of crack extensions where these functions are fitted. To avoid an influence of the process zone, when it reaches the specimens's "back side," the compliances and the capacitance are mainly fitted in the range between 0 mm and 1.6 mm crack extension.

References

[1] Haertling, G. H., 1999, "Ferroelectric Ceramics: History and Technology," J. Am. Ceram. Soc., **82**(4), pp. 797–818.
[2] Freiman, S. W., and Pohanka, R. C., 1989, "Review of Mechanically Related Failures of Ceramic Capacitors," J. Am. Ceram. Soc., **72**(12), pp. 2258–2263.
[3] Suo, Z., Kuo, C.-M., Barnett, D. M., and Willis, J. R., 1992, "Fracture Mechanics for Piezoelectric Ceramics," J. Mech. Phys. Solids, **40**(4), pp. 739–765.
[4] McMeeking, R. M., 1989, "Electrostrictive Stresses Near Crack-Like Flaws," ZAMP, **40**, pp. 615–627.
[5] McMeeking, R. M., 2001, "Towards a Fracture Mechanics for Brittle Piezoelectric and Dielectric Materials," Int. J. Fract., **108**(1), pp. 25–41.
[6] Guiu, F., Algueró, M., and Reece, M. J., 2003, "Crack Extension Force and Rate of Mechanical Work of Fracture in Linear Dielectrics and Piezoelectrics," Philos. Mag., **83**(7), pp. 873–888.
[7] Zhang, T. Y., Zhao, M., and Tong, P., 2002, "Fracture of Piezoelectric Ceramics," Adv. Appl. Mech., **38**, pp. 147–289.
[8] Park, S., and Sun, C.-T., 1995, "Fracture Criteria for Piezoelectric Ceramics," J. Am. Ceram. Soc., **78**(6), pp. 1475–1480.
[9] Tobin, A. G., and Pak, Y. E., 1993, "Effect of Electric Fields on Fracture Behavior of PZT Ceramics," Proc. SPIE, **1916**, pp. 78–86.
[10] Wang, H., and Singh, R. N., 1997, "Crack Propagation in Piezoelectric Ceramics: Effects of Applied Electric Fields," J. Appl. Phys., **81**(11), pp. 7471–7479.
[11] Lynch, C. S., 1998, "Fracture of Ferroelectric and Relaxor Electro-Ceramics: Influence of Electric Field," Acta Mater., **46**(2), pp. 599–608.
[12] Fu, R., and Zhang, T. Y., 2000, "Effects of an Electric Field on the Fracture Toughness of Poled Lead Zirconate Titanate Ceramics," J. Am. Ceram. Soc., **83**(5), pp. 1215–1218.
[13] Schneider, G. A., and Heyer, V., 1999, "Influence of the Electric Field on Vickers Indentation Crack Growth in $BaTiO_3$," J. Eur. Ceram. Soc., **19**, pp. 1299–1306.
[14] Schneider, G. A., Felten, F., and McMeeking, R. M., 2003, "The Electrical Potential Difference Across Cracks in PZT Measured by Kelvin Probe Microscopy and the Implications for Fracture," Acta Mater., **51**, pp. 2235–2241.
[15] Balke, H., Kemmer, G., and Drescher, J., 1997, "Some Remarks on Fracture Mechanics of Piezoelectric Solids," *Proceedings of the International Conference and Exhibition of Micro Materials'97*, B. Michel and T. Winkler, eds., pp. 398–401.
[16] Haug, A., and McMeeking, R., 2006, "Cracks With Surface Charge in Poled Ferroelectrics," Eur. J. Mech. A/Solids, **25**, pp. 24–41.
[17] Landis, C. M., 2004, "Energetically Consistent Boundary Conditions for Electromechanical Fracture," Int. J. Solids Struct., **41**, pp. 6291–6315.
[18] Jelitto, H., Felten, F., Häusler, C., Kessler, H., Balke, H., and Schneider, G. A., 2005, "Measurement of Energy Release Rates for Cracks in PZT Under Electromechanical Loads," Electroceramics 2004, J. Eur. Ceram. Soc., **25**, pp. 2817–2820.
[19] Sakai, M., and Bradt, R. C., 1986, "Graphical Methods for Determining the Nonlinear Fracture Parameters of Silica and Graphite Refractory Composites," *Fourth International Symposium on the Fracture Mechanics of Ceramics*, VPI, Chicago, June 19–21, 1985, Plenum Press, New York, Vol. 7, pp. 127–142.
[20] Rose, L. R. F., and Swain, M. V., 1986, "Two R-Curves for Partially Stabilized Zirkonia," J. Am. Ceram. Soc., **69**(3), pp. 203–207.
[21] Kreher, W. S., 2002, "Influence of the Domain Switching Zones on the Fracture Toughness of Ferroelectrics," J. Mech. Phys. Solids, **50**, pp. 1029–1050.
[22] Suo, Z., 1991, "Mechanics Concepts for Failure in Ferroelectric Ceramics,"

Smart Structures and Materials, ASME 1991, AD-Vol. 24/AMD-Vol. 123, pp. 1–6.
[23] Jelitto, H., Keßler, H., Schneider, G. A., and Balke, H., 2004, "Fracture Behavior of Poled Piezoelectric PZT Under Mechanical and Electrical Loads," J. Eur. Ceram. Soc., **25**(5), pp. 749–757.
[24] Kübler, J., 1998, "Bestimmung der Bruchzähigkeit keramischer Werkstoffe mit der SEVNB Methode: Resultate eines VAMAS/ESIS Ringversuches," in *Proceedings of the Werkstoffwoche*, EMPA, Dubendorf, Switzerland.
[25] Kübler, J., 2001, "Fracture Toughness of Ceramics Using the SEVNB Method: From a Preliminary Study to a Standard Test Method," in *Fracture Resistance Testing of Monolithic and Composite Brittle Materials, ASTM STP 1409*, J. A. Salem, M. G. Jenkins, and G. D. Quinn, eds., American Society for Testing and Materials, West Conshohocken, PA.
[26] Fett, T., Munz, D., and Thun, G., 1995, "Evaluation of Bridging Parameters in Aluminas From *R*-Curves by Use of the Fracture Mechanical Weight Function," J. Am. Ceram. Soc., **78**(4), pp. 949–951.
[27] Jelitto, H., Felten, F., and Schneider, G. A., 2005, "Experimenteller Aufbau zur Messung der Energiefreisetzungsrate für Risswachstum in PZT unter elektromechanischer Last," DVM-Bericht 237, 37. Tagung des DVM-Arbeitskreises Bruchvorgänge, Technische Sicherheit, Zuverlässigkeit und Lebensdauer, pp. 365–372.
[28] Heyer, V., Schneider, G. A., Balke, H., Drescher, J., and Bahr, H.-A., 1998, "A Fracture Criterion for Conducting Cracks in Homogeneously Poled Piezoelectric PZT-PIC151 Ceramics," Acta Mater., **46**(18), pp. 6615–6622.
[29] Muñoz-Saldaña, J., Schneider, G. A., and Eng, L. M., 2001, "Stress Induced Movement of Ferroelastic Domain Walls in $BaTiO_3$ Single Crystals Evaluated by Scanning Force Microscopy," Surf. Sci., **480**, pp. L402–L410.
[30] Kemmer, G., 2000, "Berechnung von elektromagnetischen Intensitätsparametern bei Rissen in Piezokeramiken," Fortschritt-Berichte VDI, Reihe **18**, Nr. 261, VDI Verlag, Düsseldorf (in German), p. 33.
[31] Kessler, H., Balke, H., Jelitto, H., and Schneider, G. A., 2004, "An Approximation for Electrically Semipermeable Edge Cracks and its Application to Fracture Analysis of PZT," Proc. Appl. Math. Mech., **4**, pp. 282–283.
[32] Kounga Njiwa, A. B., Lupascu, D. C., and Rödel, J., 2004, "Crack Tip Switching Zone in Ferroelectric Ferroelastic Materials," Acta Mater., **52**, pp. 4919–4927.
[33] Hackemann, S., and Pfeiffer, W., 2003, "Domain Switching in Process Zones of PZT: Characterization by Microdiffraction and Fracture Mechanical Methods," J. Eur. Ceram. Soc., **23**, pp. 141–151.
[34] Kolleck, A., 2000, "Einfluß der ferroelastischen Domänenschaltprozesse auf die Bruchzähigkeit und Bruchfestigkeit von $BaTiO_3$ und PZT," Fortschritt-Berichte VDI, Reihe **5**, Nr. 614, VDI Verlag, Düsseldorf (in German), pp. 159–160.
[35] Hwang, S. C., Lynch, C. S., and McMeeking, R. M., 1995, "Ferroelectric/Ferroelastic Interactions and a Polarization Switching Model," Acta Metall. Mater., **43**(5), pp. 2073–2084.